

# Decoding Complex Compositions in Topologically Close-Packed Nanoplates of Magnesium Alloys: A High-Throughput Route to Stable Precipitates

Junyuan Bai<sup>1</sup>, Xueyong Pang<sup>1,2\*</sup>, Gaowu Qin<sup>1,3,4\*</sup>

<sup>1</sup>Key Laboratory for Anisotropy and Texture of Materials (Ministry of Education), School of Materials Science and Engineering, Northeastern University, Shenyang 110819, China

<sup>2</sup>State Key Laboratory of Rolling and Automation, Northeastern University, Shenyang 110819, China

<sup>3</sup>Institute of Materials Intelligent Technology, Liaoning Academy of Materials, Shenyang 110004, China

<sup>4</sup>Research Center for Metal Wires, Northeastern University, Shenyang 110819 China

## Abstract:

Coherent topologically close-packed (TCP) nanoplates in magnesium alloys can effectively improve strength and creep resistance. However, the formation mechanisms of several metastable TCP nanoplates remain unclear, and the traditional trial-and-error methods hinder the rapid discovery of novel TCP precipitate-strengthened Mg alloys. In this study, using density functional theory calculations to construct convex hull diagrams and evaluate phase stability, our results reveal that the metastable  $\beta'_2$  nanoplates in Mg-Zn alloys adopt the Mg(Mg, Zn)<sub>2</sub> composition rather than pure MgZn<sub>2</sub>, resolving the longstanding puzzle of why stable MgZn<sub>2</sub> manifests as metastable nanoplates during Mg-Zn alloy aging. By integrating the thermodynamic and kinetic conditions for TCP precipitation, we developed a two-step high-throughput screening strategy, identifying 43 previously unreported TCP nanoplates in a series of Mg alloys. These findings highlight the critical need for precise compositional characterization of nanoprecipitates and establish a theoretical framework for designing creep-resistant Mg alloys containing TCP nanoplates.

**Key words:** High-throughput screening; DFT calculations; Coherent TCP precipitates; Mg alloys;

Corresponding author.

Email: [pangxueyong@mail.neu.edu.cn](mailto:pangxueyong@mail.neu.edu.cn) (X.Y. Pang)  
[qingw@smm.neu.edu.cn](mailto:qingw@smm.neu.edu.cn) (G. W. Qin)

Magnesium alloys, as the lightest structural metallic materials, have attracted considerable research attention for their applications in aerospace and automotive industries, wherein weight reduction is crucial for lowering energy consumption and CO<sub>2</sub> emissions. In Mg-alloy development, precipitation hardening is often recognized as an effective strengthening strategy, achieved by forming dense, coherent nanoprecipitates during aging treatments [1]. Among these nanoprecipitates, coherent topologically close-packed (TCP) nanoplates along  $\{0001\}_{\text{hcp}}$  basal planes are particularly significant, as they not only provide exceptional strength enhancement but also improve creep resistance, making them ideal for elevated-temperature applications [1–4]. These TCP nanoplates have been identified across various alloy systems, including stable phases like Mg<sub>2</sub>Ca and Al<sub>2</sub>Ca phases in Mg-Ca-(Al) alloys[5–7], metastable  $\beta'_2$ -MgZn<sub>2</sub> phase in Mg-Zn alloys[8,9], and single unit-cell height  $\gamma''$  metastable phases in Mg-RE (rare earth)-(Zn, Ag) series alloys[4,10,11]. Given the outstanding performance of TCP nanoplates in Mg alloys, the systematic identification of alloy systems capable of forming TCP nanoplates has become a crucial priority in Mg alloy development.

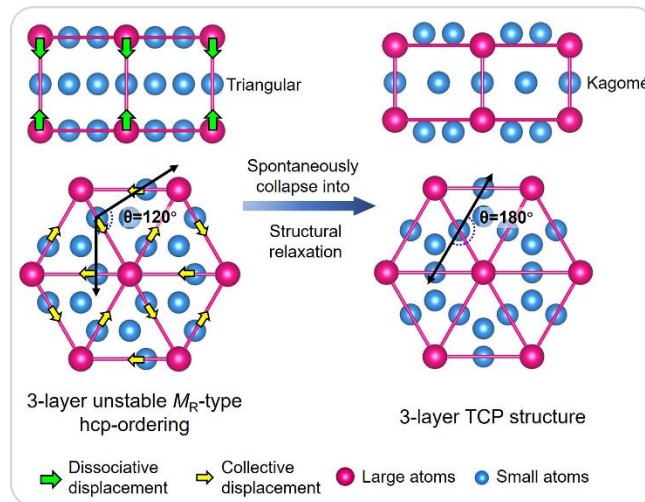


**Figure 1.** Schematic illustration of the spontaneous transformation of unstable 3-layer  $M_R$ -type hcp-ordering into a 3-layer TCP structure upon structural relaxation[12].

However, traditional trial-and-error methods are costly and inefficient for rapid alloy development. Although experimental phase diagrams and density functional theory (DFT)-calculated convex hull diagrams provide thermodynamic insights into equilibrium or metastable phases[13], they cannot determine whether a TCP phase can precipitate from

the parent matrix (a process intricately associated with kinetics) and what its resulting morphology will be. Our recent study[12] reveals that the full structural evolution pathway of TCP nanoplates within the hcp-Mg matrix is governed by the formation of 3-layer  $\{0001\}_{\text{hcp}}$ -oriented unstable solute clusters (designated as  $M_{\text{R}}$ -type hcp-ordering, Fig. 1), involving only shuffle-based displacements. During aging, under thermal fluctuations, once solute clusters evolve into the 3-layer  $M_{\text{R}}$ -type structures at a specific moment, they will spontaneously collapse into a TCP structure. Remarkably, this structural instability of specific solute clusters can be identified by structural relaxation in DFT calculations, establishing a kinetic criterion for TCP formation: if the 3-layer  $M_{\text{R}}$ -type hcp-ordering fails to induce hcp $\rightarrow$ TCP transitions upon structural relaxation, coherent TCP nanoplates cannot form kinetically.

Meanwhile, understanding the formation mechanism of TCP nanoplates from a thermodynamic perspective is also crucial. Here, we first use several common TCP nanoplates to elucidate the thermodynamic conditions for the precipitation of stable and metastable TCP nanoplates from typical dilute Mg alloys and explain the physical mechanism behind complex experimental phenomena. For stable/equilibrium phase precipitation, taking the  $\text{Mg}_2\text{Ca}$  and  $\text{Al}_2\text{Ca}$  phases in Mg-Ca-(Al) alloys as examples, we reconstructed the 0 K Mg-Ca and Mg-Al-Ca convex hull diagrams (see Fig. 2) using structural data from the Open Quantum Materials Database (OQMD)[14,15]. Convex hull analysis is a powerful method for evaluating phase stability. A phase is thermodynamically stable if its formation energy at a given composition is lower than that of all other phases of the same composition and any linear combination of energies of other phases in the phase space. The collection of all stable phases in a given phase space constitutes the convex hull, while phases located above the convex hull are thermodynamically unstable. The parameter  $E_{\text{hull}}$  measures the distance from the convex hull line and quantifies thermodynamic stability, with stable phases residing exactly on the hull ( $E_{\text{hull}}=0.0$  eV/atom) and metastable/unstable phases located above it ( $E_{\text{hull}}>0.0$  eV/atom). According to convex hull theory[16], in binary or ternary systems, unstable phases with compositions between stable phases will decompose into their neighboring stable phases, while those above a stable phase with identical composition will transform into that stable phase.

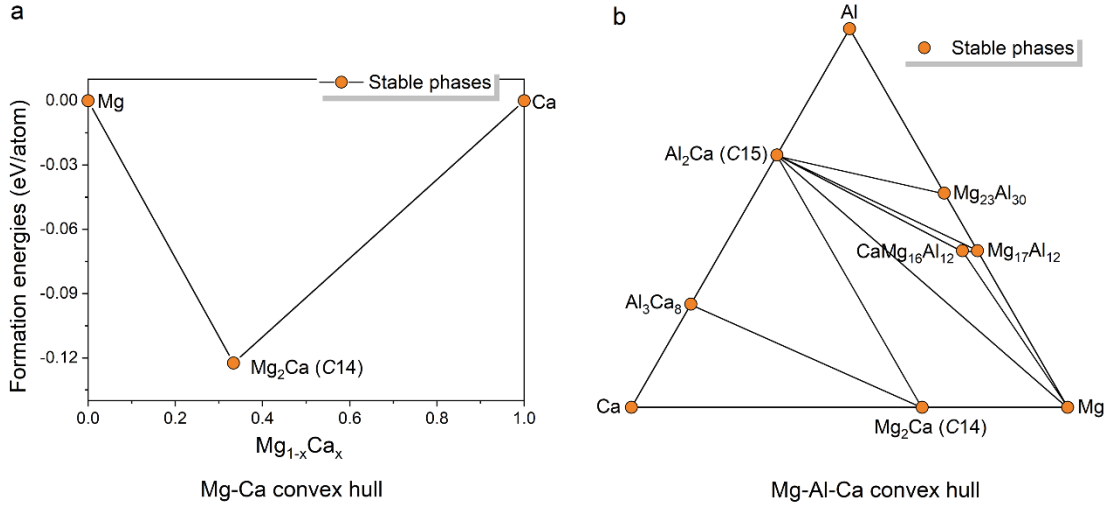


**Figure 2.** DFT-calculated zero-temperature Mg-Ca and Mg-Al-Ca convex hull diagrams.

Figure 2 shows that both  $\text{Mg}_2\text{Ca}$  with a  $C14$  structure and  $\text{Al}_2\text{Ca}$  with a  $C15$  structure lie on the convex hull, indicating that these two Laves structures are stable phases. Additionally, they also form a tie-line with Mg. A tie-line represents a straight line connecting two stable phases on a convex hull diagram, meaning that two phases can coexist. Therefore, Mg-Ca-(Al) alloys of suitable compositions thermodynamically favor the precipitation of stable  $\text{Mg}_2\text{Ca}$  and  $\text{Al}_2\text{Ca}$  phases during aging. In convex hull diagrams, precipitation of stable TCP phase from the parent Mg matrix not only demands that phase displays  $E_{\text{hull}}=0.0$  eV/atom but also forms a tie-line with Mg. In contrast, the thermodynamic precipitation mechanism of metastable TCP nanoplates is more intricate. Here, we first aim to explain why the originally stable  $\text{MgZn}_2$  phase in the Mg-Zn system occurs in the form of metastable  $\beta'_2$ - $\text{MgZn}_2$  nanoplates during the aging of Mg-Zn alloys.

The experimental Mg-Zn phase diagram[17] and the Mg-Zn convex hull diagram (see Fig. 3b) both indicate that the  $\text{MgZn}_2$ - $C14$  structure is a stable phase. According to the established thermodynamic conditions for stable-phase precipitation, this  $\text{MgZn}_2$ - $C14$  phase should form a tie-line with Mg. Instead, there are  $\text{Mg}_{21}\text{Zn}_{25}$  and  $\text{Mg}_4\text{Zn}_7$  stable phases situated between  $\text{MgZn}_2$ - $C14$  and Mg, preventing the precipitation of a stable  $\text{MgZn}_2$ - $C14$  phase from Mg-Zn alloys. However, recent experiments [9,18] commonly suggest the precipitation sequence in Mg-Zn alloys as supersaturated solid solution (S.S.S)  $\rightarrow$  GP zones  $\rightarrow \beta'_1 \rightarrow \beta'_2$  ( $\text{MgZn}_2$  nanoplates)  $\rightarrow \beta$ - $\text{Mg}_{21}\text{Zn}_{25}$ , with  $\beta'_2$ - $\text{MgZn}_2$  nanoplates clearly identified as metastable intermediates. This naturally raises the question of why the

originally stable  $\text{MgZn}_2$  phase forms during the aging of Mg-Zn alloys and exists in a metastable form.

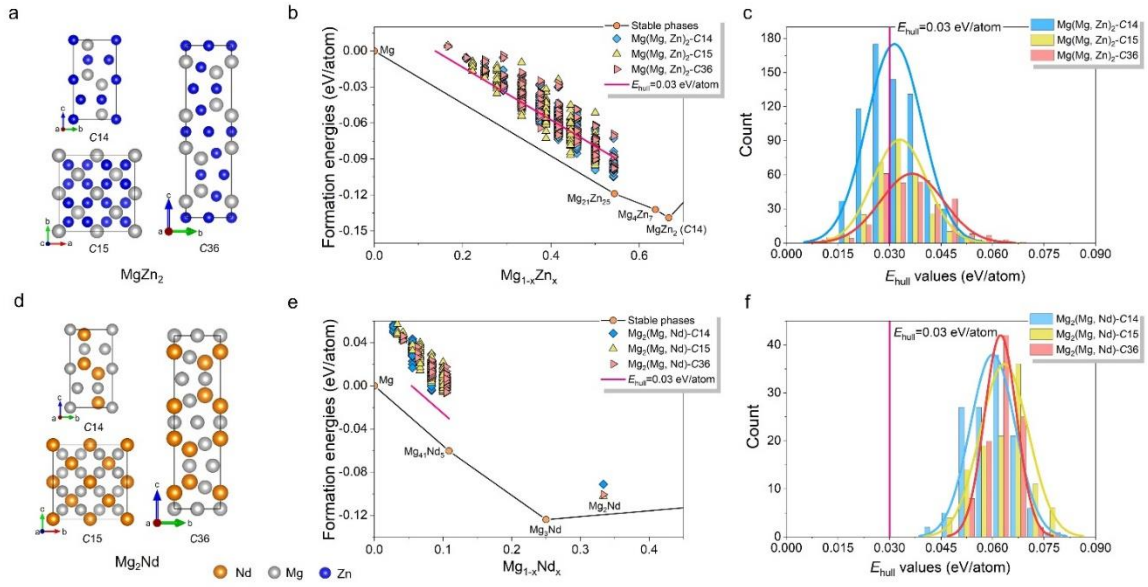


**Figure 3.** a. Atomic configurations of C14, C15, and C36-structured  $\text{MgZn}_2$  phase. b. DFT-calculated Mg-Zn convex hull diagram. c. The distribution statistics of  $E_{\text{hull}}$  values for C14, C15, and C36-based  $\text{Mg}(\text{Zn}, \text{Mg})_2$  structures. d. Atomic configurations of C14, C15, and C36-structured  $\text{Mg}_2\text{Nd}$  phase. e. DFT-calculated Mg-Nd convex hull diagram. f. The distribution statistics of  $E_{\text{hull}}$  values for C14, C15, and C36-based  $\text{Mg}_2(\text{Mg}, \text{Nd})$  structures.

In reality, nanosized precipitates often have non-stoichiometric compositions with excess matrix elements, as evidenced in systems like the  $\text{Al}_2\text{Ca}$  phase in Mg-Al-Ca alloys[19],  $\text{Al}_3\text{Sc}$  in Al-Sc alloys[20], and  $\eta$ - $\text{MgZn}_2$  phases in Al-Mg-Zn alloys[21,22]. Our recent research[12] demonstrates that TCP precipitation in the Mg matrix follows a nonclassical nucleation mechanism, where  $\text{hcp} \rightarrow \text{TCP}$  transitions mainly rely on the distribution of larger atoms in the nucleus rather than smaller ones. For example, during the formation of the  $\text{MgZn}_2$  phase (see Fig. S5), an inhomogeneous nucleus with Mg occupying anti-sites (Mg in Zn positions) can still trigger  $\text{hcp} \rightarrow \text{TCP}$  transitions. Given the nonclassical nucleation characteristics of TCP formations and the constraints of precipitation dynamics, realistic TCP nanoplates readily retain excess matrix Mg. In this context, the metastable  $\beta'_2$ - $\text{MgZn}_2$  nanoplates may also incorporate excess Mg, resulting in  $\text{Mg}(\text{Zn}, \text{Mg})_2$  stoichiometry. To evaluate the thermodynamic feasibility of  $\text{Mg}(\text{Zn}, \text{Mg})_2$  precipitation, we mixed varying amounts of Mg into the Zn positions within the three basic C14, C15, and C36 Laves structures (Fig. 3a). The formation energies of these  $\text{Mg}(\text{Zn},$

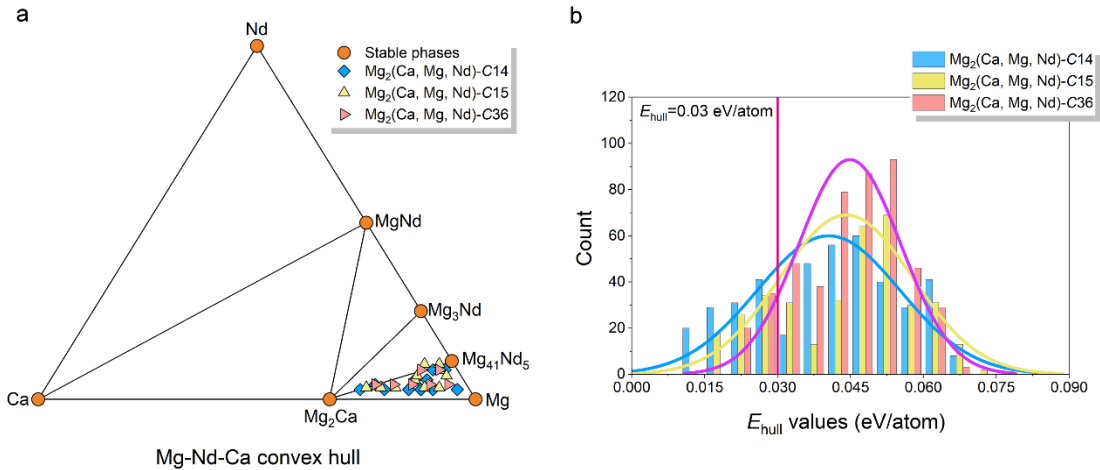
Mg)<sub>2</sub> structures were plotted on the Mg-Zn convex hull diagram to assess their phase stability. The Method section in Supplementary Information details the generation of various Mg(Zn, Mg)<sub>2</sub> structures, and the distribution statistics of their  $E_{\text{hull}}$  values are shown in Fig. 3c.

Figure 3b shows that the formation energies of all Mg(Zn, Mg)<sub>2</sub> structures lie above the convex hull line, indicating their metastable nature.  $E_{\text{hull}}$  is typically utilized as an indicator of phase stability to predict the formability of a material, where lower  $E_{\text{hull}}$  values suggest higher thermodynamic feasibility. Although the exact boundary distinguishing formable and non-formable materials remains undefined, a general threshold of  $E_{\text{hull}} \leq 0.03$  eV/atom is often considered a rule of thumb for the possible formation of metastable phases[16,23]. In Fig. 3c, a large proportion of Mg(Zn, Mg)<sub>2</sub> structures (where excess Mg atoms occupy Kagomé layers), including C14, C15, and C36 types, fall below this threshold. This distribution proves the thermodynamic feasibility of metastable Mg(Zn, Mg)<sub>2</sub> precipitation and predicts that C14, C15, and C36 structures could all present in  $\beta'_2$  nanoplates. Experimental observations[24] have reported  $\beta'_2$  nanoplates with both C14 and C15 structures. Therefore, we rectify that the stoichiometry of metastable  $\beta'_2$  nanoplates should be Mg(Zn, Mg)<sub>2</sub> rather than pure MgZn<sub>2</sub>. Moreover, careful characterization of compositions is crucial for both stable and metastable nanoprecipitates, particularly in identifying the incorporation of matrix elements, although this is always an experimental challenge.

This study further extends to elucidate the thermodynamic precipitation mechanism of metastable Mg<sub>2</sub>Nd Laves nanoplates, which exhibit unique system-dependent formation behavior. A striking observation is that these metastable Mg<sub>2</sub>Nd exclusively appear in the Mg-Nd-Ca ternary system[25], while remaining absent in binary Mg-Nd alloys. In Mg-Nd binary alloys, the reported final equilibrium precipitate is Mg<sub>41</sub>Nd<sub>5</sub>[18,26], consistent with the Mg-Nd convex hull diagram (see Fig. 3e), where Mg<sub>41</sub>Nd<sub>5</sub> is the stable phase forming a tie-line with Mg. Since the metastable Mg<sub>2</sub>Nd lies outside the Mg<sub>41</sub>Nd<sub>5</sub>-Mg region, its precipitation from Mg-Nd alloys is thermodynamically impossible. When further considering whether nonclassical nucleation behavior (with Mg occupying Nd positions) could facilitate the precipitation of metastable Mg<sub>2</sub>(Nd, Mg) phases, our evaluation of

phase stability for C14, C15, and C36-derived  $\text{Mg}_2(\text{Nd}, \text{Mg})$  structures (Fig. 3e, f) shows that most have positive formation energies and  $E_{\text{hull}}$  values well above 0.03 eV/atom. Thus, the precipitation of metastable  $\text{Mg}_2(\text{Nd}, \text{Mg})$  nanoplates from Mg-Nd alloys is thermodynamically unfeasible.

In Mg-Nd-Ca ternary alloys, we found that the formation of  $\text{Mg}_2(\text{Ca}, \text{Nd}, \text{Mg})$  metastable structures by incorporating Nd and excess Mg into  $\text{Mg}_2\text{Ca}$  nanoplates is thermodynamically feasible. The Mg-Nd-Ca convex hull diagram (Fig. 4a) shows an Mg- $\text{Mg}_2\text{Ca}$ - $\text{Mg}_{41}\text{Nd}_5$  triangle on the Mg-rich side. When introducing Nd and Mg into Ca positions and generating C14, C15, and C36-based  $\text{Mg}_2(\text{Nd}, \text{Mg})$  structures, where their compositions require to lie within the Mg- $\text{Mg}_2\text{Ca}$ - $\text{Mg}_{41}\text{Nd}_5$  triangle, the  $E_{\text{hull}}$  values of generated  $\text{Mg}_2(\text{Nd}, \text{Mg})$  structures have a large amount of portion fall below 0.03 eV/atom. This demonstrates the thermodynamic feasibility of metastable  $\text{Mg}_2(\text{Nd}, \text{Mg})$  precipitation. Thus, under the structural templating of the stable  $\text{Mg}_2\text{Ca}$  phase, the formation of metastable TCP nanoplates with complex compositions is accessible. Experimentally, when using high-angle annular dark-field scanning transmission electron microscopy (HAADF-STEM) to characterize nanoprecipitates, the high Z-contrast of Nd easily causes researchers to focus solely on Nd, overlooking lower Z-contrast elements like Ca and Mg. We once again highlight the critical need for accurate compositional determination of nanoprecipitates.



**Figure 4.** a. DFT-calculated zero temperature Mg-Nd-Ca convex hull diagram. b. The distribution statistics of  $E_{\text{hull}}$  values for C14, C15, and C36-based  $\text{Mg}_2(\text{Ca}, \text{Mg}, \text{Nd})$  structures.

Although metastable TCP nanoplates in Mg alloys may offer temporary creep-

resistance improvements, stable TCP nanoplates are more desirable for developing Mg alloys with superior long-term high-temperature creep resistance. This study devises a two-step screening strategy (Fig. 5) to identify Mg alloy systems capable of forming stable TCP nanoplates. By combining thermodynamic and kinetic conditions for TCP precipitation, this strategy utilizes DFT-calculated convex hull diagrams from the OQMD[14,15] to search for stable TCP phases forming a tie-line with Mg, followed by evaluating the structural stability of corresponding  $M_R$ -type  $X$ -ordering to determine the kinetic feasibility of TCP formation. TCP phases in Mg alloys, including Laves ( $AB_2$ -type) and Laves-like ( $AB_5$ ,  $AB_3$ , and  $A_2B_7$ -types) phases, can be categorized into three groups: Mg-containing binary phases (e.g.,  $Mg_2Ca$ ) in binary alloys, Mg-free binary (e.g.,  $Al_2Ca$ ) and Mg-containing ternary phases (e.g.,  $LaMg_2Cu_9$ ) in ternary alloys. A total of 64 Mg- $X$  binary and 2022 Mg- $X$ - $Y$  ternary convex hull diagrams from the OQMD were employed in this screening process.

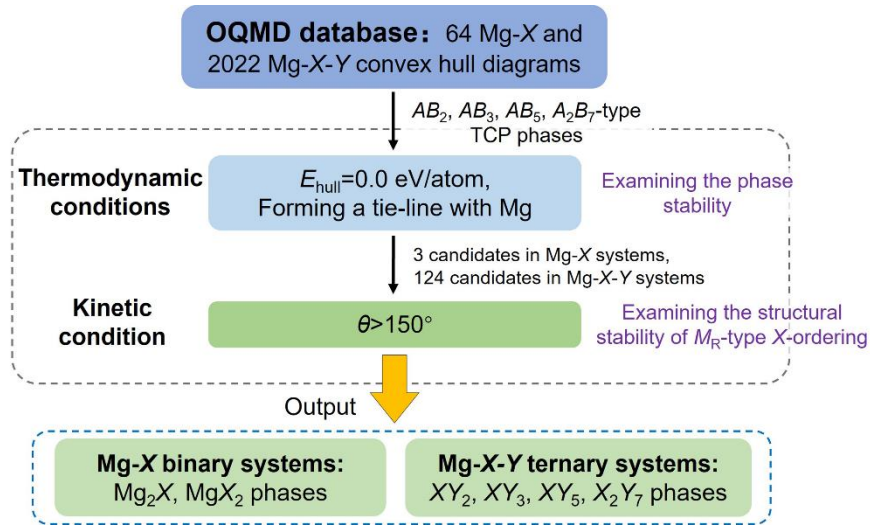


**Figure 5.** A two-step screening strategy to identify effective alloying elements in Mg- $X$  binary and Mg- $X$ - $Y$  ternary alloys that can form coherent stable TCP nanoplates.

During the second-step screening, since the nonclassical nucleation nature in  $hcp \rightarrow TCP$  transformations dictates that Mg-free TCP phase nucleation predominantly depends on the distribution of large atoms instead of small ones[27], only  $M_R$ -type  $X$ -ordering needs to be examined in Mg- $X$ - $Y$  alloys (where  $X$  denotes large atoms and  $Y$  small atoms), obviating the need for extensive examinations of  $M_R$ -type  $X$ - $Y$ -orderings across



124 candidates. Given that hcp $\rightarrow$ TCP transitions involve a lattice transformation from triangular to kagomé structures (which changes the  $\theta$  value from  $120^\circ$  to  $180^\circ$ [27]), as shown in Fig. 1, a larger change in  $\theta$  value within our model correlates with a higher tendency for TCP formation. Hence, we adopted  $\theta$  as a structural indicator to examine the structural stability of  $M_R$ -type  $X$ -orderings, setting a threshold of  $\theta > 150^\circ$  based on the observed clustering distribution of  $\theta$  values across various Mg- $X$  combinations (see Fig. S4). For this screening step, we used 162-atom models (Fig. S1 (a-b)) with different  $M_R$ -type  $X$ -ordering sizes for structural relaxations. Further details on DFT calculations and models are provided in the Supplementary Information.

**Table 1.** High-throughput screening results of stable TCP nanoplates in Mg- $X$  binary and Mg- $X$ - $Y$  ternary alloys.

No.	Mg- $X$ binary systems	Structural type	No.	$X$	Mg- $X$ - $Y$ systems	Structural type
1	Mg <sub>2</sub> Ca <sup>†</sup>	C14	21		HoFe <sub>2</sub>	C15
2	Mg <sub>2</sub> Yb	C14	22		HoFe <sub>3</sub>	$AB_3$
3	MgCo <sub>2</sub>	C36	23		HoOs <sub>2</sub>	C14
				Ho		
			24		HoRe <sub>2</sub>	C14
			25		HoTc <sub>2</sub>	C14
			26	K	KNa <sub>2</sub>	C14
			27	La	LaAl <sub>2</sub>	C15
			28	Nd	NdAl <sub>2</sub>	C15
			29	Pm	PmAl <sub>2</sub>	C15
			30	Pr	PrAl <sub>2</sub>	C15
			31		SmAl <sub>2</sub>	C15
			32	Sm	SmOs <sub>2</sub>	C14
			33		TbAl <sub>2</sub>	C15
			34	Tb	TbOs <sub>2</sub>	C14
			35		Th <sub>2</sub> Fe <sub>7</sub>	$A_2B_7$
			36		ThFe <sub>5</sub>	$AB_5$
			37	Th	ThOs <sub>2</sub>	C14
			38		ThRe <sub>2</sub>	C14
			39		ThTc <sub>2</sub>	C14
No.	$X$	Mg- $X$ - $Y$ systems	Structural type			
1	Ca	CaAl <sub>2</sub> <sup>†</sup>	C15			
2	Ce	CeAl <sub>2</sub>	C15			
3		CsK <sub>2</sub>	C15			
4	Cs	CsNa <sub>2</sub>	C14			
5		DyAl <sub>2</sub>	C15			
6		DyOs <sub>2</sub>	C14			
7	Dy	DyRe <sub>2</sub>	C14			
8		DyTc <sub>2</sub>	C14			
9		ErAl <sub>2</sub>	C15			
10		ErCo <sub>2</sub>	C15			
11		ErFe <sub>2</sub>	C15			
12	Er	ErFe <sub>3</sub>	$AB_3$			
13		ErOs <sub>2</sub>	C14			
14		ErRe <sub>2</sub>	C14			
15		ErTc <sub>2</sub>	C14			

16	Eu	EuAl <sub>2</sub>	C15	40		YAl <sub>2</sub> <sup>†</sup>	C15
17		GdAl <sub>2</sub> <sup>†</sup>	C15	41	Y	YOs <sub>2</sub>	C14
18	Gd	GdOs <sub>2</sub>	C14	42		YRe <sub>2</sub>	C14
19		GdRe <sub>2</sub>	C14	43		YTe <sub>2</sub>	C14
20	Ho	HoAl <sub>2</sub>	C15	44	Yb	YbAl <sub>2</sub>	C15

<sup>†</sup> represents the TCP phase that has been observed in experiments.

Table 1 summarizes the high-throughput screening results for stable TCP phases in Mg-*X* and Mg-*X*-*Y* alloys. In binary systems, Mg<sub>2</sub>Ca, Mg<sub>2</sub>Yb, and MgCo<sub>2</sub> were identified as potential precipitates, with Mg<sub>2</sub>Ca nanoplates have been experimentally confirmed. For ternary Mg-*X*-*Y* alloys, 44 TCP phases, including Al<sub>2</sub>Ca [5], Al<sub>2</sub>Y [28], and Al<sub>2</sub>Gd [29] (Laves precipitates widely observed in previous research), were found, demonstrating the reliability of our screening approach. As TCP nanoplates are known to enhance the strength and creep resistance of Mg alloys, the newly discovered TCP phases could expand the chemical space for alloy design. Table 1 further suggests that REAl<sub>2</sub> Laves phases may widely precipitate in Mg-RE-Al series alloys. In these alloys [30], TCP nanoplates typically form at lower aging temperatures (~200°C), while at higher temperatures (~500°C), long-period stacking ordered (LPSO) phases become more common.

A distinct class of single-unit-cell-thick metastable TCP phases, termed  $\gamma''$  phases, are often observed in Mg-RE-Zn (Ag) alloys. Owing to their unique ability to maintain constant thickness during aging, these  $\gamma''$  phases have received widespread attention over the past decade[4,10,18]. Regarding their thermodynamic origins, Zhao et al.[31] recently suggest that  $\gamma''$  phases in Mg-Nd-Ag alloys act as metastable intermediates for the equilibrium non-TCP NdAgMg<sub>11</sub> phase, based on HAADF-STEM observations and atomic-scale energy-dispersive X-ray spectroscopy. This reveals a unique precipitation pathway where non-TCP equilibrium phases use TCP-structured intermediates to mediate their precipitation. Applying the two-step screening strategy, we extended our search to potential stable TCP phases in hcp-structured Ti and Zr alloys in the Supplementary Information. Our results indicate that only the TiCr<sub>2</sub> and ZrMn<sub>2</sub> Laves phases (see Table S1) may precipitate from Ti-Cr and Zr-Mn binary alloys. This is mainly because, under the formation of unstable  $M_R$ -type hcp-ordering, all large elements in the Ti (Zr) matrix cannot interact with the surrounding matrix to induce hcp→TCP transitions (see Fig. S4a), unlike

those in the soft Mg matrix. Meanwhile, we emphasize that these screening results offer only preliminary guidance for future experimental explorations, as many intricate factors, such as solid solubility of relevant adding elements, alloy composition, thermal processing history, etc., also significantly affect the precipitation of TCP plates.

In this study, using DFT calculations to construct convex hull diagrams and assess phase stability, we rectified that the metastable  $\beta'_2$  nanoplates in Mg-Zn alloys are Mg(Mg, Zn)<sub>2</sub> rather than pure MgZn<sub>2</sub>. We also clarified that the stoichiometry of the experimentally observed metastable Mg<sub>2</sub>Nd phase in Mg-Nd-Ca alloys is Mg<sub>2</sub>(Nd, Mg, Ca) and explained why this phase does not form in binary Mg-Nd alloys. This highlights the importance of accurately determining the composition of nanoprecipitates in experiments. Furthermore, by integrating the thermodynamic and kinetic conditions for TCP precipitation, we developed a two-step high-throughput screening strategy to identify stable TCP nanoplates in Mg alloys. The newly discovered TCP phases may facilitate the design of high-strength and creep-resistant Mg alloys. These findings enhance our atomic-level understanding of precipitation behavior in various hcp-based alloys and lay a foundation for designing advanced materials incorporating coherent TCP nanoplates.

## References:

- [1] J.F. Nie, Physical Metallurgy of Light Alloys, in: Physical Metallurgy: Fifth Edition, Elsevier Inc., 2014: pp. 2009–2156.
- [2] J.F. Nie, X. Gao, S.M. Zhu, Enhanced age hardening response and creep resistance of Mg-Gd alloys containing Zn, *Scr Mater* 53 (2005) 1049–1053.
- [3] X. Gao, S.M. Zhu, B.C. Muddle, J.F. Nie, Precipitation-hardened Mg-Ca-Zn alloys with superior creep resistance, *Scr Mater* 53 (2005) 1321–1326.
- [4] J.F. Nie, K. Oh-ishi, X. Gao, K. Hono, Solute segregation and precipitation in a creep-resistant Mg-Gd-Zn alloy, *Acta Mater* 56 (2008) 6061–6076.
- [5] M. Li, D. Xie, J. Li, H. Xie, Q. Huang, H. Pan, G. Qin, Realizing ultra-fine grains and ultra-high strength in conventionally extruded Mg-Ca-Al-Zn-Mn alloys: The multiple roles of nano-precipitations, *Mater Charact* 175 (2021) 111049.
- [6] A. Suzuki, N.D. Saddock, J.W. Jones, T.M. Pollock, Solidification paths and eutectic intermetallic phases in Mg-Al-Ca ternary alloys, *Acta Mater* 53 (2005) 2823–2834.
- [7] A. Suzuki, N.D. Saddock, J.R. TerBush, B.R. Powell, J.W. Jones, T.M. Pollock,

- Precipitation strengthening of a Mg-Al-Ca - Based AXJ530 die-cast alloy, *Metall Mater Trans A Phys Metall Mater Sci* 39 A (2008) 696–702.
- [8] X. Gao, J.F. Nie, Characterization of strengthening precipitate phases in a Mg-Zn alloy, *Scr Mater* 56 (2007) 645–648.
- [9] J. Buha, Reduced temperature (22-100 °C) ageing of an Mg-Zn alloy, *Materials Science and Engineering: A* 492 (2008) 11–19.
- [10] J. Bai, X. Pang, X. Meng, H. Xie, H. Pan, Y. Ren, M. Jiang, G. Qin, Anomalous crystal structure of  $\gamma''$  phase in the Mg-RE-Zn(Ag) series alloys: Causality clarified by ab initio study, *J Mater Sci Technol* 36 (2020) 167–175.
- [11] H. Xie, H. Pan, Y. Ren, S. Sun, L. Wang, H. Zhao, B. Liu, X. Qi, G. Qin, Magnesium alloys strengthened by nanosaucer precipitates with confined new topologically close-packed structure, *Cryst Growth Des* 18 (2018) 5866–5873.
- [12] J. Bai, H. Xie, X. Pang, M. Jiang, G. Qin, Structural pathway for nucleation and growth of topologically close-packed phase from parent hexagonal crystal, *Acta Mater* 274 (2024) 119999.
- [13] C.J. Bartel, Review of computational approaches to predict the thermodynamic stability of inorganic solids, *J Mater Sci* 57 (2022) 10475–10498.
- [14] J.E. Saal, S. Kirklin, M. Aykol, B. Meredig, C. Wolverton, Materials design and discovery with high-throughput density functional theory: The open quantum materials database (OQMD), *JOM* 65 (2013) 1501–1509.
- [15] S. Kirklin, J.E. Saal, B. Meredig, A. Thompson, J.W. Doak, M. Aykol, S. Rühl, C. Wolverton, The Open Quantum Materials Database (OQMD): Assessing the accuracy of DFT formation energies, *NPJ Comput Mater* 1 (2015) 15010.
- [16] C.J. Bartel, Review of computational approaches to predict the thermodynamic stability of inorganic solids, *J Mater Sci* 57 (2022) 10475–10498.
- [17] H. Okamoto, Comment on Mg-Zn (Magnesium-Zinc), *Journal of Phase Equilibria* 15 (1994) 129–130.
- [18] J.F. Nie, Precipitation and hardening in magnesium alloys, *Metall Mater Trans A Phys Metall Mater Sci* 43 (2012) 3891–3939.
- [19] A. Suzuki, N.D. Saddock, J.W. Jones, T.M. Pollock, Structure and transition of eutectic (mg,al)<sub>2</sub>ca laves phase in a die-cast mg-al-ca base alloy, *Scr Mater* 51 (2004)

1005–1010.

- [20] A. Orthacker, G. Haberfehlner, J. Taendl, M.C. Poletti, B. Sonderegger, G. Kothleitner, Diffusion-defining atomic-scale spinodal decomposition within nanoprecipitates, *Nat Mater* 17 (2018) 1101–1107.
- [21] J.Z. Liu, J.H. Chen, Z.R. Liu, C.L. Wu, Fine precipitation scenarios of AlZnMg(Cu) alloys revealed by advanced atomic-resolution electron microscopy study: Part II: Fine precipitation scenarios in AlZnMg(Cu) alloys, *Mater Charact* 99 (2015) 142–149.
- [22] J.Z. Liu, J.H. Chen, D.W. Yuan, C.L. Wu, J. Zhu, Z.Y. Cheng, Fine precipitation scenarios of AlZnMg(Cu) alloys revealed by advanced atomic-resolution electron microscopy study Part I: Structure determination of the precipitates in AlZnMg(Cu) alloys, *Mater Charact* 99 (2015) 277–286.
- [23] G.G.C. Peterson, J. Brgoch, Materials discovery through machine learning formation energy, *JPhys Energy* 3 (2021).
- [24] W. Lou, H. Xie, X. Zhao, J. Bai, H. Zhang, Y. Wang, X. Li, H. Pan, Y. Ren, G. Qin, Variable precipitation behaviors of Laves phases in an ultralight Mg-Li-Zn alloy, *Journal of Magnesium and Alloys* 11 (2023) 2018–2026.
- [25] W.R. Ren, Z.Q. Li, A.P. Zhang, H.W. Chen, Precipitation of Mg<sub>2</sub>Nd Laves phases in a Mg-Nd-Ca alloy, *Vacuum* 218 (2023).
- [26] A.R. Natarajan, E.L.S. Solomon, B. Puchala, E.A. Marquis, A. Van Der Ven, On the early stages of precipitation in dilute Mg-Nd alloys, *Acta Mater* 108 (2016) 367–379.
- [27] S.J. Kang, T.H. Kim, C.W. Yang, J.I. Lee, E.S. Park, T.W. Noh, M. Kim, Atomic structure and growth mechanism of T1 precipitate in Al-Cu-Li-Mg-Ag alloy, *Scr Mater* 109 (2015) 68–71.
- [28] Y. Chen, Q. Li, Y. Li, W. Zheng, J. Wang, X. Zeng, Phase equilibria of long-period stacking ordered phase in the ternary Mg-Y-Al alloys, *J Mater Sci Technol* 126 (2022) 80–92.
- [29] X. Dong, L. Feng, S. Wang, G. Ji, A. Addad, H. Yang, E.A. Nyberg, S. Ji, On the exceptional creep resistance in a die-cast Gd-containing Mg alloy with Al addition, *Acta Mater* 232 (2022).

- [30] H. Zhang, C.Q. Liu, Y.M. Zhu, H.W. Chen, L. Bourgeois, J.F. Nie, Revisiting building block ordering of long-period stacking ordered structures in Mg–Y–Al alloys, *Acta Mater* 152 (2018) 96–106.
- [31] X. Zhao, Z. Li, A. Zhang, L. Hao, H. Chen, J.F. Nie, Atomic-scale investigation of precipitate phases in QE22 Mg alloy, *J Mater Sci Technol* 177 (2024) 114–127.

### **Acknowledgments**

This research is supported by the National Key Research and Development Program of China (2023YFB3710902), Fundamental Research Funds for the Central Universities of China (N2102011, N2007011, N160208001), and National 111 Project (B20029).

### **Author contributions**

G. Qin and J. Bai conceived the original idea and designed the work. J. Bai conducted the simulations with help from X. Pang. J. Bai wrote the paper. G. Qin supervised the project and revised the manuscript.

**Declaration of Competing Interests:** The authors declare that they have no known competing financial interests or personal relationships that could have appeared to influence the work reported in this paper.

### **Data availability**

The data that support the findings of this study are available from the corresponding author upon reasonable request.

### **Code availability**

The code in this study is available from the authors upon reasonable request.

**Supplementary Information for**  
**Decoding Complex Compositions in Topologically Close-Packed**  
**Nanoplates of Magnesium Alloys: A High-Throughput Route to Stable**  
**Precipitates**

Junyuan Bai<sup>1</sup>, Xueyong Pang<sup>1,2\*</sup>, Gaowu Qin<sup>1,3,4\*</sup>

<sup>1</sup>*Key Laboratory for Anisotropy and Texture of Materials (Ministry of Education), School of Materials Science and Engineering, Northeastern University, Shenyang 110819, China*

<sup>2</sup>*State Key Laboratory of Rolling and Automation, Northeastern University, Shenyang 110819, China*

<sup>3</sup>*Institute of Materials Intelligent Technology, Liaoning Academy of Materials, Shenyang 110004, China*

<sup>4</sup>*Research Center for Metal Wires, Northeastern University, Shenyang 110819 China*

Corresponding author.

Email: [pangxueyong@mail.neu.edu.cn](mailto:pangxueyong@mail.neu.edu.cn) (X.Y. Pang)

[qingw@smm.neu.edu.cn](mailto:qingw@smm.neu.edu.cn) (G. W. Qin)

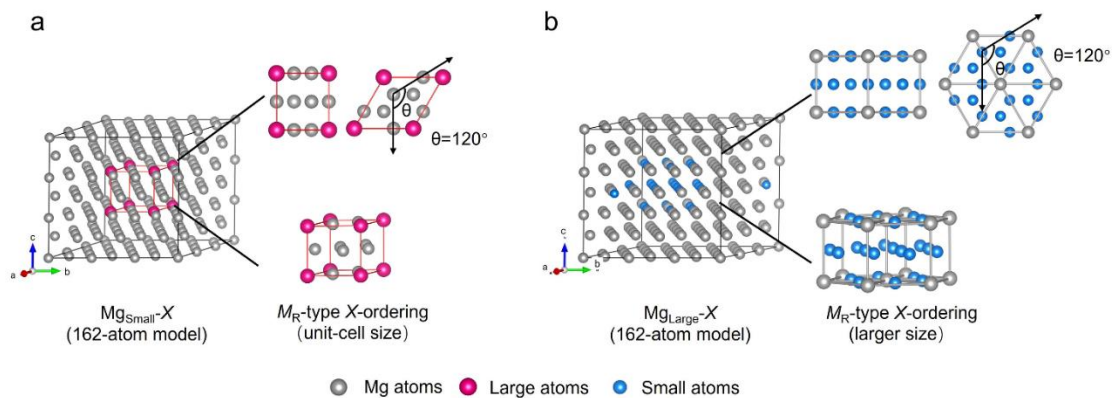


**Figure S1. a-b.** Atomic structural models in the situations of  $Mg_{Small-X}$  and  $Mg_{Large-X}$ . The Mg, large, and small atoms are marked with grey, dark-pink, and light-blue balls, respectively.

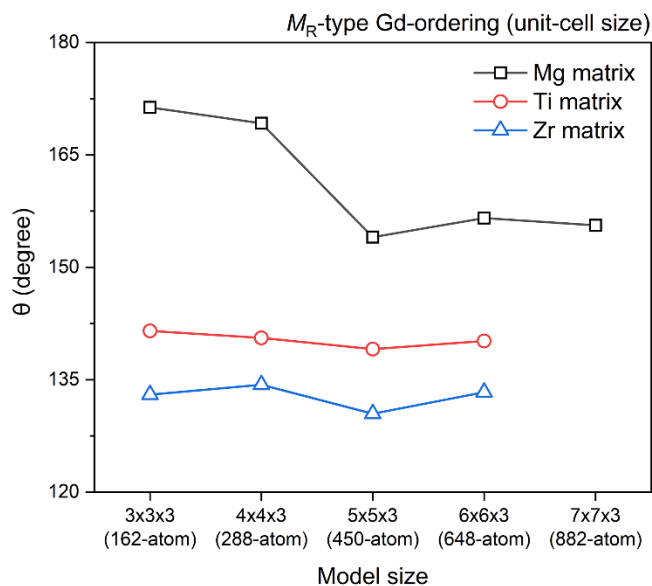


**Figure S2.** Convergence tests of  $\theta$  value for model size across different matrices.



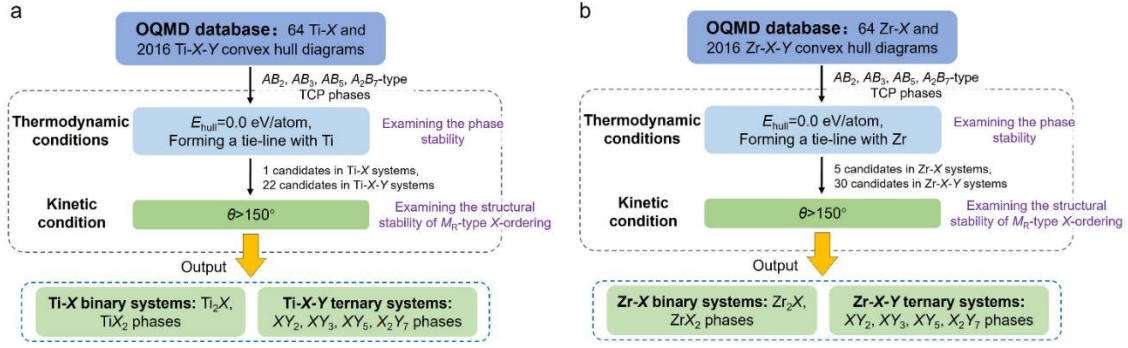


**Figure S3.** A two-step screening strategy to identify effective alloying elements in (Ti, Zr)-*X* binary and (Ti, Zr)-*X*-*Y* ternary alloys that can form coherent stable TCP nanoplates.

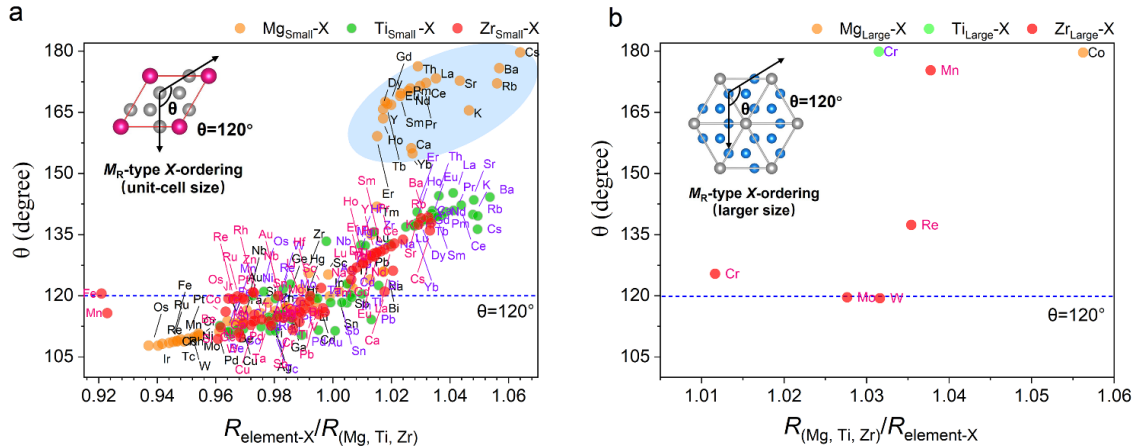


**Figure S4. a.** The variation of  $\theta$  value of relaxed  $M_R$ -type *X*-ordering with calculated radius ratios ( $R_{\text{element-X}}/R_{(\text{Mg, Ti, Zr})}$ ) for (Mg, Ti, Zr)<sub>Small</sub>-*X* scenarios. A unit-cell structure of  $M_R$ -type hcp-ordering is shown in the inset of the panel, and the pink and grey balls represent the large and small atoms, respectively. **b.** The variation of  $\theta$  value of relaxed  $M_R$ -type *X*-ordering with calculated radius ratios ( $R_{(\text{Mg, Ti, Zr})}/R_{\text{element-X}}$ ) for (Mg, Ti, Zr)<sub>Large</sub>-*X* scenarios. A large-sized structure of  $M_R$ -type *X*-ordering is shown in the inset of the panel, and the grey and blue balls represent the large and small atoms, respectively.

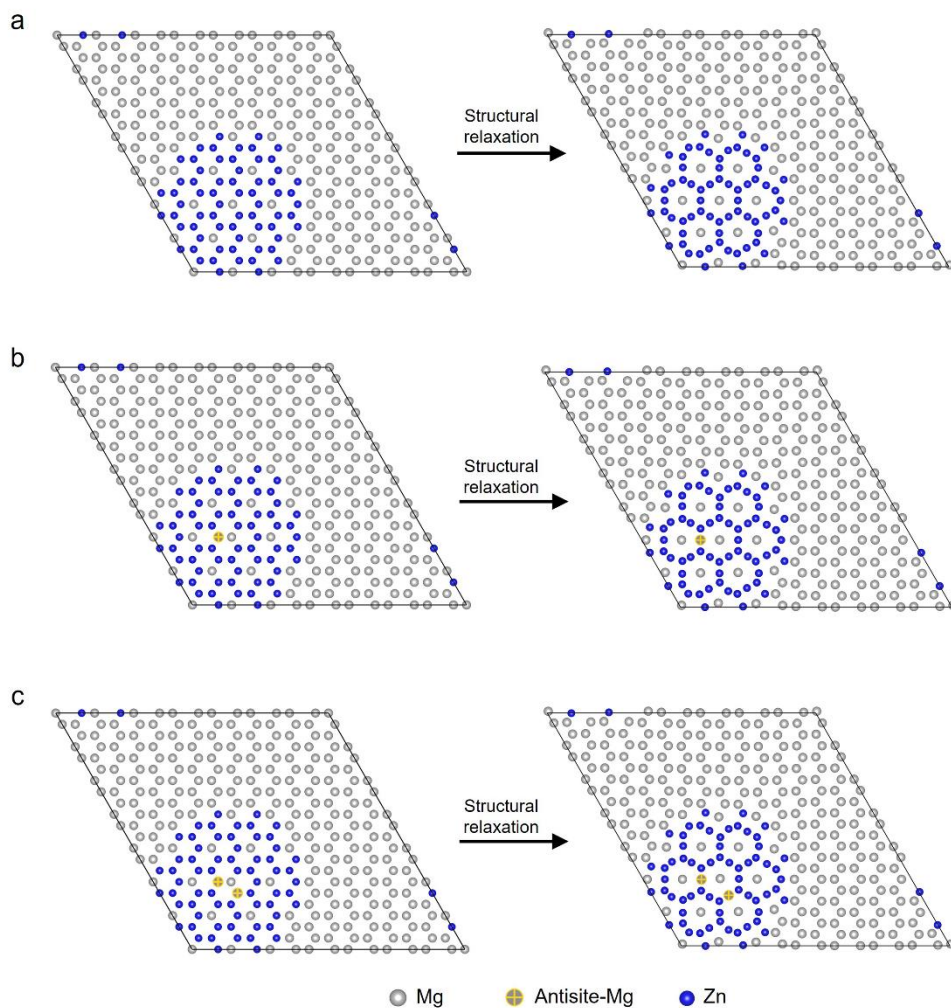


**Figure S5.** Schematic illustration of nonclassical nucleation behavior of  $\text{MgZn}_2$  nucleation in the Mg matrix, depicting nuclei with (a) non antisite Mg atoms, (b) one antisite Mg atom, and (c) two antisite Mg atoms. An 882-atom model was employed for DFT calculations.

**Table S1.** High-throughput screening results of the stable TCP nanoplates in Ti-*X* and Zr-*X* binary alloys.

No.	Ti- <i>X</i> binary systems	Structural type	No.	Zr- <i>X</i> binary systems	Structural type
1	TiCr <sub>2</sub>	C15	1	ZrMn <sub>2</sub>	C15

## Methods

DFT calculations were conducted using the Vienna *ab initio* simulation package (VASP)[1,2] employing Blochl’s projector augmented wave (PAW) potential method[3]. The exchange-correlation energy functional was described with the generalized gradient approximation (GGA) as parameterized by Perdew-Burke-Ernzerhof (PBE)[4]. The frozen core pseudopotentials were used for RE elements, as these pseudopotentials have been shown to replicate the thermodynamics and elastic properties of rare-earth intermetallics [5,6]. A 520 eV plane wave cutoff was adopted, with convergence criteria for energy and atomic force set as  $10^{-6}$  eV and  $10^{-2}$  eV/Å, respectively. Partial occupancies were determined using the first-order Methfessel-Paxton method with a smearing width of 0.2 eV[7]. Relaxations of atomic coordinates and optimizations of the shape and size of the model were adopted for all calculations. A  $\Gamma$ -centered *k*-point mesh of  $18 \times 18 \times 10$  was adopted for the HCP primitive cell, with other supercells appropriately scaled to maintain a constant *k*-point density. Large numbers of symmetrically distinct Mg(Zn, Mg)<sub>2</sub>, Mg<sub>2</sub>(Nd, Mg), and Mg<sub>2</sub>(Nd, Ca, Mg) structures based on C14, C15, and C36 types were generated with the Clusters Approach to Statistical Mechanics (CASM) code[8].

The unit-cell structure of *M<sub>R</sub>*-type hcp-ordering was constructed based on their *a*-vector, *b*-vector, and *c*-vector parallel to the  $[10\bar{1}0]_{\text{hcp}}$ ,  $[01\bar{1}0]_{\text{hcp}}$  and  $[0001]_{\text{hcp}}$  directions, respectively. During screening, we chose the  $\theta$  value as a structural indicator to determine whether there were hcp→TCP transitions. In Fig. S2, we tested  $\theta$  variation across different model sizes for three types of matrices. The results indicate that while smaller models, like the 162-atom ( $3 \times 3 \times 3$ ) model (Fig. S1), amplify the  $\theta$  value for the Mg matrix scenario due to periodic interactions, our calculations (Fig. S4a) based on this 162-atom model still display a clustered data distribution that can effectively identify candidate elements from a large pool of elements. Hence, to balance computational accuracy and cost, we employed this 162-atom ( $3 \times 3 \times 3$ ) model containing *M<sub>R</sub>*-type *X*-ordering with one unit-cell size or larger-sized (i.e., clusters in a 3D environment) for high-throughput screenings of hcp-Mg, Ti, and Zr alloys.

Models containing  $M_R$ -type  $X$ -ordering with a single unit-cell size (Fig. S1a,  $Mg_{\text{Small-X}}$  situations) were employed to examine Mg-free binary phases such as the  $Al_2Ca$  phase, while the models containing the  $M_R$ -type  $X$ -ordering with larger size (Fig. S1b,  $Mg_{\text{Large-X}}$  situations) were used to examine the Mg-containing phases where Mg acts as the large atoms, e.g.,  $MgCo_2$  phases. The same rule was also applied to hcp-based Ti and Zr matrices. The calculated structural stability results of these  $M_R$ -type  $X$ -ordering across  $Mg_{\text{Small-X}}$  and  $Mg_{\text{Large-X}}$  situations within the Mg matrix, as well as in the matrices of hcp-based Ti, and Zr, are shown in Fig. S4. The atomic radii of different elements  $R_{\text{element}}$  in various hcp-matrix were calculated by measuring the average nearest distance of neighboring matrix atoms in a 54-atom model.

The formation energy  $E_f$  of a configuration  $A_xB_y$ , for instance, was calculated relative to the zero kelvin total energies of pure elements A and B as follows:

$$E_f = \frac{E(A_xB_y) - N_x E_A - N_y E_B}{N_x + N_y} \quad (\text{S-1})$$

Where  $E(A_xB_y)$  denotes the total energies of a configuration, and  $E_A$  and  $E_B$  are the total energies per atom for pure elements  $A$  and  $B$ , respectively.  $N_x$  and  $N_y$  represent the number of elements  $A$  and  $B$  in the configuration. In this way, the formation energy of a configuration with ternary or more constituents can be obtained. The zero temperature convex hull diagrams were constructed by using the *pymatgen* code [9].

### Supplementary References:

- [1] G. Kresse, J. Hafner, Ab initio molecular dynamics for open-shell transition metals, *Phys Rev B* 48 (1993) 13115–13118.
- [2] G. Kresse, J. Hafner, Ab initio molecular dynamics for liquid metals, *Phys Rev B* 47 (1993) 558–561.
- [3] P.E. Blöchl, Projector augmented-wave method, *Phys Rev B* 50 (1994) 17953–17979.
- [4] J.P. Perdew, K. Burke, M. Ernzerhof, Generalized gradient approximation made simple, *Phys Rev Lett* 77 (1996) 3865–3868.
- [5] M.C. Gao, A.D. Rollett, M. Widom, Lattice stability of aluminum-rare earth binary systems: A first-principles approach, *Phys Rev B Condens Matter Mater Phys* 75 (2007).
- [6] L. Huber, I. Elfimov, J. Rottler, M. Militzer, Ab initio calculations of rare-earth diffusion in magnesium, *Phys Rev B Condens Matter Mater Phys* 85 (2012) 1–7.

- [7] M. Methfessel, A.T. Paxton, High-precision sampling for Brillouin-zone integration in metals, *Phys Rev B* 40 (1989) 3616–3621.
- [8] B. Puchala, J.C. Thomas, A.R. Natarajan, J.G. Goiri, S.S. Behara, J.L. Kaufman, A. Van der Ven, CASM — A software package for first-principles based study of multicomponent crystalline solids, *Comput Mater Sci* 217 (2023).
- [9] S.P. Ong, W.D. Richards, A. Jain, G. Hautier, M. Kocher, S. Cholia, D. Gunter, V.L. Chevrier, K.A. Persson, G. Ceder, Python Materials Genomics (pymatgen): A robust, open-source python library for materials analysis, *Comput Mater Sci* 68 (2013) 314–319.